Performance Enhancement of Optical Comb Based Microwave Photonic Filter by Machine Learning Technique

Run-Kai Shiu, You-Wei Chen, Peng-Chun Peng, Justin Chiu, Qi Zhou, Tsu-Lin Chang, Shuyi Shen, Jyun-Wei Li, and Gee-Kung Chang, *Fellow, IEEE*

***Abstract*—Machine learning technique is employed to design a microwave photonic filter (MPF) consisting of an optical comb generator and a phase modulator (PM), to realize centralized management of radio signal delivery in optical networks. The proposed comb generator successfully generates up to 103 optical carriers with adjustable wavelength spacing and number of optical carriers. It exhibits large tunability, flat band response and high tone-to-noise ratio. Thus, the proposed optical comb-based filter is capable to provide flexible tunability with respect to its center frequency and 3-dB bandwidth. In our experimental setup, different wavelength spacing settings and number of optical carriers are fed into the PM for modulation and their corresponding frequency responses are measured by a network analyzer. The experimental data have been analyzed to correlate with the simulation results and theoretical predictions. Besides, a subcarrier multiplexing (SCM) technique can be applied to a multi-user optical system incorporating the proposed filter since its frequency response is varied by the accumulated dispersion. After measuring the characteristic of the proposed filter, a set of frequency responses is collected and fed into the convolutional neural network (CNN) model to obtain the inverse mapping between frequency response to the wavelength spacing and fiber length. As a result, the well-trained model can successfully predict the wavelength spacing and fiber length with high accuracy.**

***Index Terms*—Microwave photonic filter, radio-over-fiber, machine learning technique.**

I. Introduction

MICROWAVE photonic filter (MPF) has gained much research interest recently since it features wide operational bandwidth, large frequency tuning range and low radio frequency-dependent loss as well as immunity to electromagnetic interference [1]–[6]. Comparing with MPF, traditional electronic filters are more difficult to achieve large tunability, high Q factor and reconfigurability. Thus, MPF is a promising technology to process microwave signals in the optical domain and the applications of MPF have been reported in radar systems, radio-astronomy and radio-over-fiber (RoF) systems [7]–[10]. Several MPF techniques have been investigated such as using a Lyot loop filter [11], broadband light source [12], Fabry-Perot filter [13], Mach-Zehnder interferometer [14], stimulated Brillouin scattering (SBS) effect [15], and micro-ring resonator (MRR) [16]–[18]. In some application scenarios, it is highly demanding that both the center frequency and 3-dB bandwidth of the MPF should be widely tunable to satisfy different demands. Therefore, to meet such requirements, a finite impulse response (FIR) MPF based on a delay-line structure is another alternative by utilizing multiple optical carriers' source and a dispersive medium [19]–[23]. Some schemes using multiple optical carriers had been proposed [24]–[27]. In [24] the adjustment to the phase shift is realized by optically pumping the tilted fiber Bragg grating (TFBG). However, this method requests a specific wavelength arrangement of the optical carriers in order to meet the linear transmission response of the TFBG which decreases the system flexibility. Moreover, the FBG is also sensitive to temperature [28] and thus it reduces the system stability. Another scheme reported in [25], proposed an MPF based on an MRR. The tunability could be achieved by allocating optical carriers on the phase transfer function of MRR to induce different phase shift. Therefore, to obtain the desired phase shift, an array of laser diodes (LDs) is needed and the wavelength setting should match certain region in the phase transfer curve of the MRR which is impractical and inflexible. The optical carriers generated by the MRR structure in [26] present a good performance of power fluctuation which is below 0.5 dB by applying feedback control calibration. The MPF constructed by the above-mentioned MRR also exhibits outstanding results by varying the tap coefficients. The wavelength spacing between each optical carrier is fixed due to the parameter of the MRR. In [27], multiple optical carriers are generated by a Brillouin-erbium fiber laser (BEFL). By launching optical carriers to the electro-optic modulator (EOM), both the center frequency and 3-dB bandwidth of the MPF can be adjusted. In order to tune the center frequency of the MPF, different types of optical fiber are required to generate different wavelength spacing, which is not practical. The 3-dB bandwidth of the MPF is changed by varying the number of wavelengths.

Manuscript received January 31, 2020; revised April 2, 2020; accepted April 16, 2020. Date of publication April 20, 2020; date of current version October 1, 2020. This work was supported by the Ministry of Science and Technology, Taiwan, under Grants MOST 108-2221-E-027-040-MY2 and MOST 108-2917-I-027 -001. *(Corresponding author: Peng-Chun Peng.)*

Run-Kai Shiu, Peng-Chun Peng, Justin Chiu, Tsu-Lin Chang, and Jyun-Wei Li are with the Department of Electro-Optical Engineering, National Taipei University of Technology, Taipei 10608, Taiwan (e-mail: t106659002@ntut.edu.tw; pcpeng@ntut.edu.tw; t107658073@ntut.edu.tw; t101658009@ntut.edu.tw; t108658001@ntut.edu.tw).

You-Wei Chen, Qi Zhou, Shuyi Shen, and Gee-Kung Chang are with the School of Electrical and Computer Engineering, Georgia Institute of Technology, Atlanta, GA 30308 USA (e-mail: yu-wei.chen@ece.gatech.edu; qi.zhou@gatech.edu; ssyzoe@gatech.edu; geekung.chang@ece.gatech.edu).

Color versions of one or more of the figures in this article are available online at https://ieeexplore.ieee.org.

Digital Object Identifier 10.1109/JLT.2020.2989210

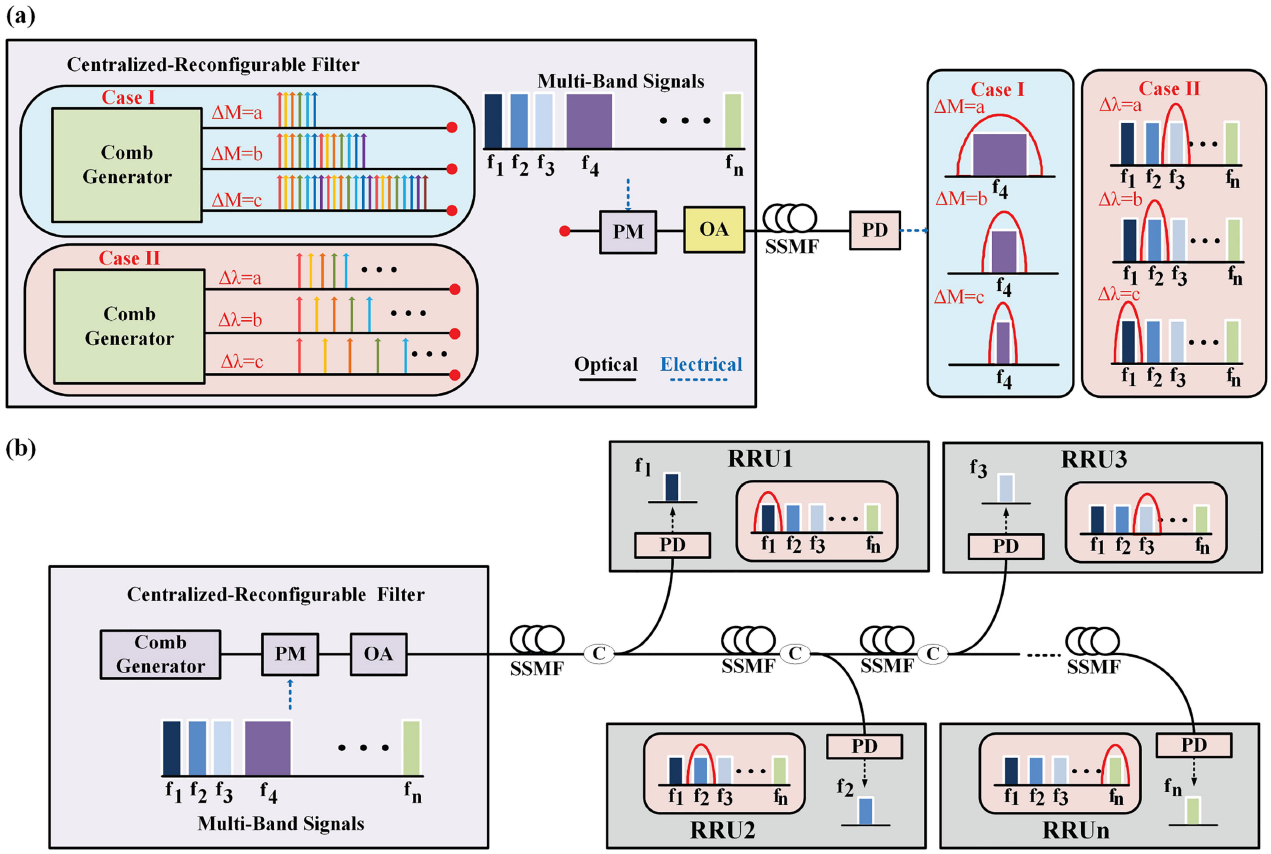

Fig. 1. Schematic diagrams of (a) the proposed centralized-reconfigurable filter and (b) a SCM-based RoF system with proposed filter for multi-user service (PM: phase modulator, OA: optical amplifier, SSMF: standard single-mode fiber, and PD: photo detector, C: coupler, RRU: remote radio unit).

However, the number of wavelengths is limited in the presented BEFL scheme which restricts the tunability of the MPF.

In this paper, an optical comb generator based on dual-parallel Mach-Zehnder modulator (DP-MZM) and a phase modulator (PM) for achieving a centralized reconfigurable MPF is proposed and experimentally demonstrated in an optical system over 50-km fiber link. The proposed optical comb generator providing up to 103 optical carriers with tunable wavelength spacing and carrier number enables the MPF to provide a large tunability. The frequency response of the proposed filter is a function of the wavelength spacing, the number of optical carriers and fiber length. Thus, by varying these three factors, we can precisely adjust the center frequency and 3-dB bandwidth of the MPF with large flexibility, and this feature can benefit the future software-defined optical network for enhancing the network flexibility [29]–[31]. However, even the MPF can be reconfigured by these three factors easily, it is hard to determine them if we designate a arbitrary transmission window of the MPF. Machine learning techniques have shown impressive performance in different applications [32]–[34], like multi-level signal recovery, precise 3D positioning, and FBG sensor system. Therefore, we apply the novel approach, using machine learning technique, to design the inverse system of the proposed MPF to enhance the performance. A multi-layer convolutional neural network (CNN) is employed to learn the inverse mapping between the frequency response and the parameters of the MPF. After the CNN model is trained, the wavelength spacing, and fiber length can be precisely predicted by the given arbitrary frequency response window through forward propagation in the multi-layer neural network.

The rest of the paper is organized as follows: Section II. shows the theoretical analysis of the proposed MPF; Section III. describes the experimental set up and results of (i) the optical comb generator and (ii) the proposed MPF; Section IV. presents the methodology and design of the proposed CNN model; Section V. depicts the conclusion of the presented work.

II. Theoretical Analysis

The proposed centralized-reconfigurable filter consists of a comb generator, a PM, an optical amplifier (OA), standard single-mode fiber (SSMF), photo detector (PD) as shown in Fig. 1(a). In the proposed scheme, a PM is used for modulation of multi-band signals with different bandwidths which will be allocated to their desired users at different radio frequencies. By tuning the center frequency and 3-dB bandwidth of the filter, we can remove the specific signal band for its dedicated subscriber for security enhancement with a physical layer control. The proposed filter is highly reconfigurable via the comb generator. For clear elaboration, we classify it into two scenarios. In case I, by increasing the number of generated optical carriers, the 3-dB bandwidth of the proposed filter is narrowing down. On the other

hand, if we fix the number of optical carriers, the center frequency of the proposed MPF can be arbitrarily shifted when we change the wavelength spacing among optical carriers as shown in case II. A concept of subcarrier multiplexing (SCM) technology based RoF system is depicted in Fig. 1(b), where RRU is the remote radio unit. Besides tuning the center frequency by the wavelength spacing, changing the accumulated dispersion value can also shift the center frequency of the proposed filter. Thus, we can distribute multi-band signals to different subscribers and achieve point-to-multipoint downstream transmission by varying the dispersion value via different lengths of SSMF.

The complete theoretical analysis of the proposed filter is described below. To derive the mathematical model of the proposed filter, we consider that there is only a single wavelength launched into the PM first.

A tunable laser (TL) with single wavelength can be expressed as $\mathrm{E(t)} = \mathrm{E}_0 e^{j\omega_0 t}$, where $\mathrm{E}_0$and $\omega_0$are the amplitude and angular frequency of the employed TL. As applying a sinusoidal radio-frequency (RF) signal to drive an externally modulated PM, the output E-field of PM is$\mathrm{E(t)} = \mathrm{E}_0 e^{j\omega_0 t} \cdot e^{jm\cos\omega_r t}$, where $m = \frac{\pi v_m}{v_\pi}$and $\omega_r$denote the modulation index and the angular frequency of the RF signal applied to PM, respectively. By using the Jacobi-Anger Expansion, and only considering small signal conditions, the output E-filed of PM becomes

$$\begin{aligned}\mathrm{E(t)} &= \mathrm{E}_0 e^{j\omega_0 t} \cdot \sum_{n=-\infty}^{\infty} j^n J_n(m) \mathrm{e}^{jn\omega_r t} \\ &= \mathrm{E}_0 e^{j\omega_0 t} \begin{bmatrix} J_0(m) \\ +J_1(m)\mathrm{e}^{j(\omega_r t+\frac{\pi}{2})} \\ -J_1(m)\mathrm{e}^{j(-\omega_r t-\frac{\pi}{2})} \end{bmatrix} \end{aligned} \tag{1}$$

where Jn is the first kind of Bessel function. Since the SSMF is a dispersive device, the phase delay between center carrier and first-order sidebands will be induced after they are transmitted through the fiber. Thus, (1) should be rewritten as

$$E(t) = \mathrm{E}_0 e^{j\omega_0 t} \begin{bmatrix} J_0(m)e^{j\theta_0} \\ J_1(m)e^{j(\omega_r t+\frac{\pi}{2}+\theta_1)} \\ -J_1(m)e^{j(-\omega_r t-\frac{\pi}{2}+\theta_2)} \end{bmatrix} \tag{2}$$

where θ_0, θ_1 and θ_2 are the phase delays of center carrier, positive and negative first-order sidebands, respectively. The phase delays induced by a SSMF of these three optical components can be expressed as [35]

$$\begin{aligned} \theta_0 &= z\beta(\omega_0) \\ \theta_1 &= z\beta(\omega_0) + z\dot{\beta}(\omega_0)(\omega_r) + \frac{1}{2}z\ddot{\beta}(\omega_0)(\omega_r)^2 \\ \theta_2 &= z\beta(\omega_0) - z\dot{\beta}(\omega_0)(\omega_r) + \frac{1}{2}z\ddot{\beta}(\omega_0)(\omega_r)^2 \end{aligned} \tag{3}$$

where $\dot{\beta}(\omega_0)$ and $\ddot{\beta}(\omega_0)$ are the first and second derivatives of $\beta(\omega_0)$ in regard to ω_0 and z is the length of SSMF. After center carrier and sidebands are detected by a PD, the photo current is the multiplication of E(t) and its conjugate as

$$i_{PD} \propto \sin\left(\frac{1}{2}z\ddot{\beta}(\omega_0)(\omega_r)^2\right)\cos(\omega_0 t + \varphi) \tag{4}$$

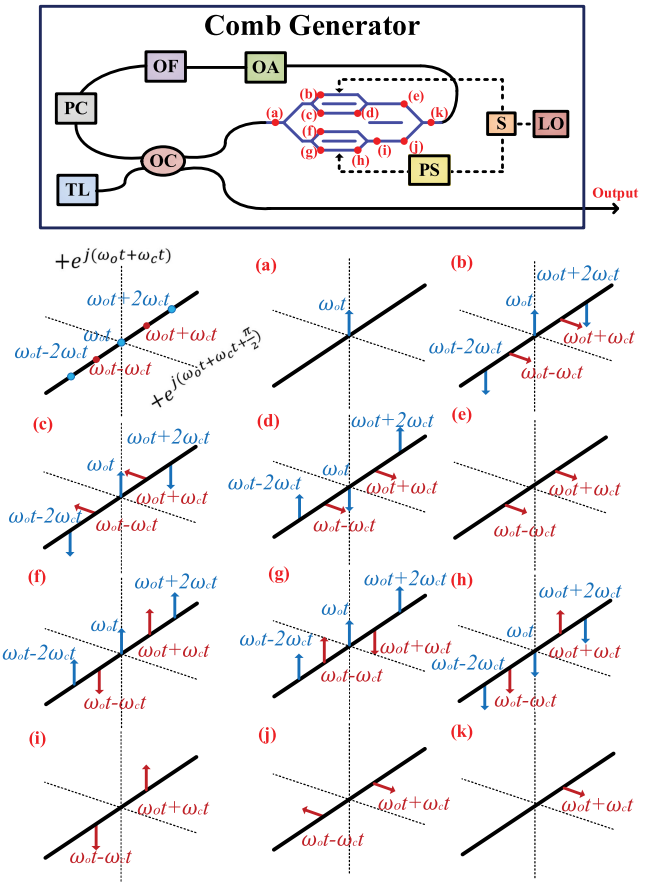

Fig. 2. Configuration of the comb generator and the schematic optical components of all corresponding points in the DP-MZM. (OC: coupler, PC: polarization controller, PS: phase shifter, S: power splitter, LO, local oscillator, and OF: optical filter).

where φ is the phase delay of the received RF signal. The fiber dispersive parameter D is the partial derivative of group delay in regard to wavelength and fiber distance, which is

$$D(\lambda_0) = \frac{\ddot{\beta}(\omega_0)(\omega_0)^2}{2\pi c} \tag{5}$$

By substituting (5) into (4), we have

$$i_{PD} \propto \sin\left(\frac{\pi c z D(\lambda_0){\omega_r}^2}{{\omega_0}^2}\right)\cos(\omega_r t + \varphi) \tag{6}$$

By applying Fourier transform to (6), we obtain the frequency response of the proposed filter considering only one wavelength as follows:

$$H_{Single}(\omega_r) \propto \sin\left(\frac{\pi c z D(\lambda_0){\omega_r}^2}{{\omega_0}^2}\right) \tag{7}$$

Equation (7) represents the dispersion induced frequency response of the PM. Now, we consider applying comb generator to launch *M* optical carriers to the PM.

Fig. 2 shows the configuration and the schematic optical components for all points relating to DP-MZM of the proposed comb generator. Comb generator is composed of a TL, a 50:50 optical coupler (OC), a DP-MZM, an OA, a tunable optical filter (OF), and a polarization controller (PC). The idea to generate

an optical comb is that we use the DP-MZM to duplicate the incident lightwave and shift its wavelength. The replica, right-shifted wavelength, is amplified by an Erbium-doped optical fiber amplifier (EDFA) for compensating the loss of wavelength transition and then it is coupled with TL by OC prior to being launched into the DP-MZM again. In the second round, the wavelength of both TL and the first replica are right-shifted by DP-MZM again and the second replica is generated. By repeating the same process for (M-1) rounds, M optical carriers are generated. The principle of generating replica with right-shifted frequency is illustrated below. Fig. 2(a) shows the TL source with amplitude E_0 and angular frequency $\omega_0$which is launched to the DP-MZM. The DP-MZM consists of three MZMs and each MZM can be regarded as two PMs [36]. After MZM1 is driven by an RF signal, the phase term of MZM1-upper PM will undergo a phase change $\phi = m\cos(\omega_c t)$. Thus, using the Jacobi-Anger Expansion and only considering the essential optical components (n < 3), the E-filed of MZM1-upper PM as shown in Fig. 2(b) can be written as

$$\begin{aligned}\mathrm{E}_{Mzm1-upper} &= \frac{1}{2}\mathrm{E}_0 e^{j\omega_0 t}\cdot e^{jm\cos\omega_c t}\\ &= \frac{1}{2}\mathrm{E}_0 e^{j\omega_0 t}\begin{Bmatrix} J_0(m)\\ +J_1(m)\mathrm{e}^{j(\omega_c t+\frac{\pi}{2})}\\ -J_1(m)\mathrm{e}^{j(-\omega_c t-\frac{\pi}{2})}\\ -J_2(m)e^{j2\omega_c t}\\ -J_2(m)e^{-j2\omega_c t}\end{Bmatrix}\end{aligned} \tag{8}$$

Because the RF signal launched to the MZM1-lower PM is opposite to that of MZM1-upper PM, the phase change of MZM1-lower PM is a πdifferent from that of MZM1-upper PM. Therefore, The E-filed of MZM1-lower PM as shown in Fig. 2(c), can be expressed as

$$\begin{aligned}\mathrm{E}_{Mzm1-lower} &= \frac{1}{2}\mathrm{E}_0 e^{j\omega_0 t}\cdot e^{jm\cos(\omega_c t+\pi)}\\ &= \frac{1}{2}\mathrm{E}_0 e^{j\omega_0 t}\begin{Bmatrix} J_0(m)\\ +J_1(m)\mathrm{e}^{j(\omega_c t+\frac{\pi}{2}+\pi)}\\ -J_1(m)\mathrm{e}^{j(-\omega_c t-\frac{\pi}{2}-\pi)}\\ -J_2(m)\mathrm{e}^{j2\omega_c t}\\ -J_2(m)\mathrm{e}^{-j2\omega_c t}\end{Bmatrix}\end{aligned} \tag{9}$$

If we bias MZM1 at V_π, the phase terms of all optical components of (9) will be shifted by π. Thus, (9) should be rewritten as

$$\mathrm{E}_{Mzm1-lower} = \frac{1}{2}\mathrm{E}_0 e^{j\omega_0 t}\begin{Bmatrix} J_0(m)\mathrm{e}^{j\pi}\\ +J_1(m)\mathrm{e}^{j(\omega_c t+\frac{\pi}{2})}\\ -J_1(m)\mathrm{e}^{j(-\omega_c t-\frac{\pi}{2})}\\ -J_2(m)\mathrm{e}^{j(2\omega_c t+\pi)}\\ -J_2(m)\mathrm{e}^{j(-2\omega_c t+\pi)}\end{Bmatrix} \tag{10}$$

Equation (10) illustrates the point(d) in Fig. 2. As shown in (11), Fig. 2(e) indicates the output E-field of MZM1 which is the combination of MZM1 upper and lower PM.

$$\begin{aligned}\mathrm{E}_{Mzm1-output} &= \frac{1}{\sqrt{2}}(\mathrm{E}_{Mzm1-upper}+\mathrm{E}_{Mzm1-lower})\\ &= \frac{1}{\sqrt{2}}\mathrm{E}_0 e^{j\omega_0 t}\left[+J_1(m)\mathrm{e}^{j(\omega_c t+\frac{\pi}{2})}-J_1(m)\mathrm{e}^{j(-\omega_c t-\frac{\pi}{2})}\right]\end{aligned} \tag{11}$$

For the MZM2, a $-\frac{\pi}{2}$ phase shift on the injected RF signal is induced via a phase shifter. Therefore, the phase change of MZM2-upper PM induced by the RF signal is $\phi = m\cos(\omega_c t-\frac{\pi}{2})$. As using the same mathematical analysis performed in MZM1, the output E-field of MZM2-upper PM (Fig. 2(f)) can be expressed as

$$\begin{aligned}\mathrm{E}_{Mzm2-upper} &= \frac{1}{2}\mathrm{E}_0 e^{j\omega_0 t}\cdot e^{jm\cos(\omega_c t-\frac{\pi}{2})}\\ &= \frac{1}{2}\mathrm{E}_0 e^{j\omega_0 t}\begin{Bmatrix} J_0(m)\\ +J_1(m)\mathrm{e}^{j\omega_c t}\\ -J_1(m)\mathrm{e}^{-j\omega_c t}\\ -J_2(m)\mathrm{e}^{j(2\omega_c t-\pi)}\\ -J_2(m)\mathrm{e}^{j(-2\omega_c t+\pi)}\end{Bmatrix}\end{aligned} \tag{12}$$

Similar to MZM1, the E-field applied to MZM2-lower PM (Fig. 2(g)) is a πdifferent from that of MZM2-upper PM. Assuming the DC bias of MZM2 is set to V_π, the output E-filed of MZM2-lower PM as shown in Fig. 2(h) is

$$\mathrm{E}_{Mzm2-lower} = \frac{1}{2}\mathrm{E}_0 e^{j\omega_0 t}\begin{Bmatrix} J_0(m)\mathrm{e}^{j\pi}\\ +J_1(m)\mathrm{e}^{j\omega_c t}\\ -J_1(m)\mathrm{e}^{-j\omega_c t}\\ -J_2(m)\mathrm{e}^{j2\omega_c t}\\ -J_2(m)\mathrm{e}^{-j2\omega_c t}\end{Bmatrix} \tag{13}$$

By the summation of (12) and (13), we obtain the output E-field of MZM2 as follows:

$$\begin{aligned}\mathrm{E}_{Mzm2-output} &= \frac{1}{\sqrt{2}}(\mathrm{E}_{Mzm2-upper}+\mathrm{E}_{Mzm2-lower})\\ &= \frac{1}{\sqrt{2}}\mathrm{E}_0 e^{j\omega_0 t}\left[+J_1(m)\mathrm{e}^{j\omega_c t}-J_1(m)\mathrm{e}^{-j\omega_c t}\right]\end{aligned} \tag{14}$$

Because the DC bias of MZM3 is set to $\frac{V_\pi}{2}$, the phase terms of all optical components of the MZM2 output port (Fig. 2(i)) will be shifted by $\frac{\pi}{2}$. Thus, Fig. 2(j), the output E-filed of MZM3-lower PM, can be expressed as

$$\begin{aligned}&\mathrm{E}_{Mzm3-lower}\\ &= \frac{1}{\sqrt{2}}\mathrm{E}_0 e^{j\omega_0 t}\left[+J_1(m)\mathrm{e}^{j(\omega_c t+\frac{\pi}{2})}-J_1(m)\mathrm{e}^{j(-\omega_c t+\frac{\pi}{2})}\right]\end{aligned} \tag{15}$$

Hence, by combining both MZM3-upper and lower PM, the replica whose frequency is located at $\omega_0 t+\omega_c t$ is generated as shown in (16).

$$\begin{aligned}\mathrm{E}_{Mzm3-output} &= \frac{1}{\sqrt{2}}(\mathrm{E}_{Mzm3-upper}+\mathrm{E}_{Mzm3-lower})\\ &= \mathrm{E}_0 e^{j\omega_0 t}J_1(m)\mathrm{e}^{j(\omega_c t+\frac{\pi}{2})}\\ &= \mathrm{E}_0 J_1(m)\mathrm{e}^{j(\omega_0 t+\omega_c t+\frac{\pi}{2})}\end{aligned} \tag{16}$$

As shown in (16), the angular frequency of the incident lightwave $\omega_0 t$ is right-shifted to $\omega_0 t+\omega_c t$.Therefore, for the *M*th optical carrier, its angular frequency will be $\omega_0 t+(M-1)\omega_c t$. According to (7), we consider launching M optical carriers into the PM instead of a single wavelength and thus (7) should be

rewritten as

$$i_{PD} \propto \sum_{m=1}^{M} \sin\left(\frac{\pi c z D(\lambda_m){\omega_r}^2}{[\omega_0+(m-1)\omega_c]^2}\right)\cdot P_m\cos(\omega_r t+\varphi_m) \tag{17}$$

where M is the number of optical carriers. We can regard the first term in (17) as the identical term for all optical carriers since the frequency spacing of all optical carriers are the same and small [37]. Thus, (17) becomes

$$i_{PD} \propto \sin\left(\frac{\pi c z D(\lambda_{ave}){\omega_r}^2}{{\omega_{ave}}^2}\right) \cdot \sum_{m=1}^{M} P_m\cos(\omega_r t+\varphi_1+\omega_r(m-1)T) \tag{18}$$

where $D(\lambda_{ave})$ is the averaged dispersion, ω_{ave} is the averaged angular frequency and T is the time interval between each optical carrier and it equals wavelength spacing multiplies the average accumulated dispersion. By applying Furrier transform to (18), the frequency response of the proposed filter based on comb generator is obtained as follows:

$$H_{Comb}(\omega_r) \propto \sin\left(\frac{\pi c z D(\lambda_{ave}){\omega_r}^2}{{\omega_{ave}}^2}\right) \cdot \sum_{m=1}^{M} P_m\cdot e\left[j\omega_r(m-1)T\right] \tag{19}$$

The frequency response of the proposed filter is governed by the number of optical carriers, the wavelength spacing and the dispersive value as shown in (19), and thus the frequency response can be tuned by these three crucial factors.

III. Experimental Set Up and Results

A. Comb Generator

Fig. 2 depicts the setup of the comb generator for the proposed filter of our experiment. After passing through the 3-dB optical coupler, the TL emitted at 1546.8 nm is launched into the DP-MZM with 3 dBm input power. Both MZM1 and MZM2 are biased at the null point while MZM3 is biased at its quadrature point. The driving RF signal frequency is 10 GHz and the phase shifter is deployed in one branch after power splitter to make sure the phase difference between the MZM1 and MZM2 inputs is $-\frac{\pi}{2}$. The EDFA output power is set to 17 dBm to compensate the loss of the loop caused by wavelength transition. By properly adjusting the OF, the number of optical carriers of comb generator from 20 to 100 can be flexibly achieved as shown in Fig. 3(a). To investigate the performance of the proposed filter, the maximum 103 optical carriers with 0.08 nm wavelength spacing are selected as shown in Fig. 3(b). The tone-to-noise ratio (TNR) of the generated 103 optical carriers is greater than 17 dB and the optical power fluctuation is below 2 dB. The power fluctuation can be improved by changing the weights of each optical carrier by using waveshaper [38].

To change the wavelength spacing of the generated optical combs, we adjust the frequency of the RF signal to 20 GHz, 15 GHz, 10 GHz and 7.5 GHz, corresponding to wavelength spacing of 0.16 nm, 0.12 nm, 0.08 nm and 0.06 nm, respectively. Fig. 4 shows the measured optical spectra from 1548 nm to 1552 nm with (a) 0.16 nm (b) 0.12 nm (c) 0.08 nm (d) 0.06 nm wavelength spacing. All the measured optical spectra have good flatness and large TNR. This can ensure the proposed MPF has large tunability since the mathematical model as shown in (19) pointing out that the number and wavelength spacing of the optical carriers are two important factors to tune the proposed filter.

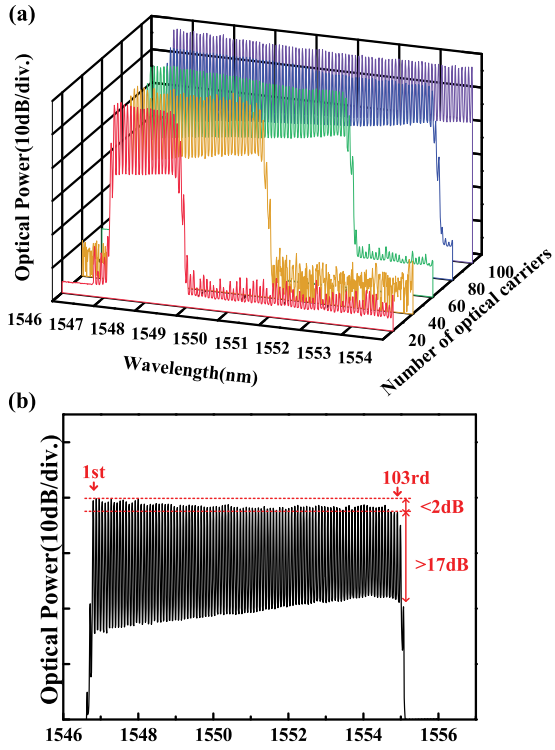

Fig. 3. Measured optical spectra of (a) 20,40,60,80, and 100 optical carriers with 0.08 nm wavelength spacing and (b) 103 optical carriers with 0.08 nm wavelength spacing.

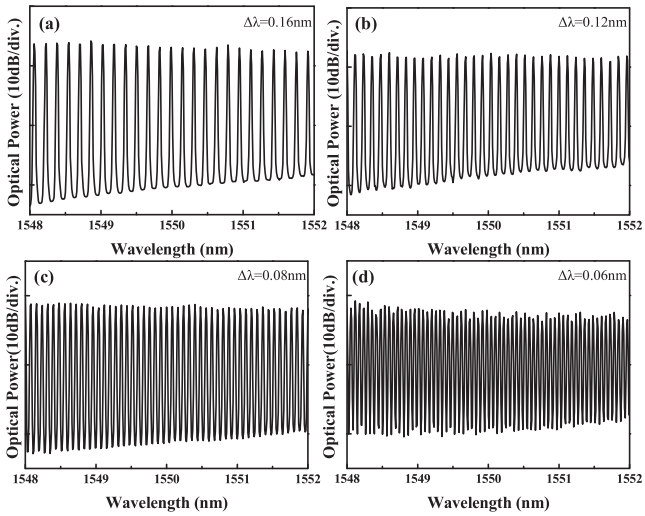

Fig. 4. Measured optical spectra of (a) 0.16 nm (b) 0.12 nm (c) 0.08 nm (d) 0.06 nm wavelength spacing.

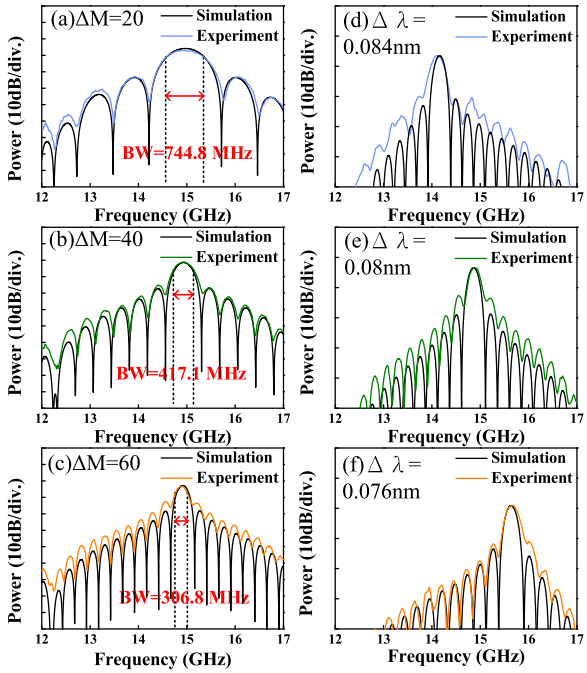

Fig. 5. Simulation and experimental results of the proposed filter considering case I (the number of optical carriers is set to (a) 20, (b) 40 and (c) 60) and case II (the wavelength spacing is set to (d) 0.084 nm (e) 0.08 nm (f) 0.076 nm).

B. MPF

To conduct the frequency response measurement for the proposed filter, the sequential microwave signals generated by the network analyzer are injected to PM to modulate all optical carriers. After 50-km SSMF transmission, all optical carriers are detected by PD and the recovered microwave signals are sent back to network analyzer to measure the frequency response. In case I, the wavelength spacing is fixed at 0.08 nm and 20, 40 and 60 optical carriers are fed into the PM, respectively. Fig. 5 (a), (b) and (c) show both experimental and simulation results of the frequency response considering different numbers of optical carriers. The simulation results correlate with the experimental results. Experimental results show the measured 3-dB bandwidth decreases from 744.8 MHz to 306.8 MHz when the number of carriers increases from 20 to 60. It is observed that the 3-dB bandwidth of the filter is decreasing as the number of optical carriers is increasing, pointing that the resolution can be improved by feeding more optical carriers to the PM.

In case II, to evaluate the tunability of center frequency of the proposed filter, the number of optical carriers is fixed to 60 while the wavelength spacing can be adjusted to match different application requirements.

Fig. 5(d), (e) and (f) illustrate the experimental and simulation results of the frequency response when we adjust the wavelength spacing to 0.084 nm, 0.08 nm and 0.076 nm, respectively. Fig. 5(d) indicates the center frequency of the proposed filter is 14.08 GHz and it is shifted to 14.86 GHz and 15.66 GHz when the wavelength spacing is changed to 0.08 nm and 0.076 nm as shown in Fig. 5(e) and (f). Same as the case I, the simulation results agree with experimental results in case II.

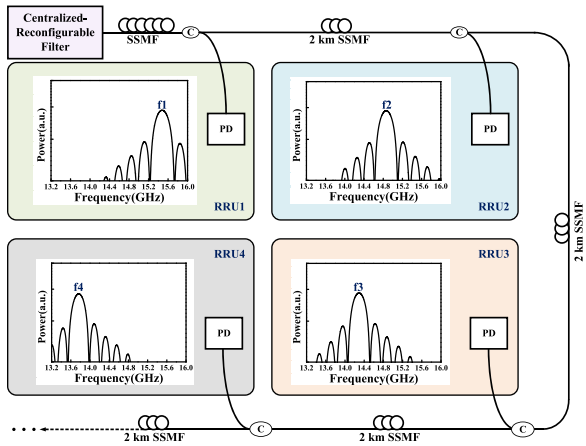

Fig. 6. Simulation of frequency response of the proposed filter versus different fiber lengths.

Based on the well-matched simulation results, we further simulate the multi-service application scenario of the proposed filter. Fig. 6 shows the simulated frequency response versus different transmission distances. The center frequency of the proposed filter is shifted to the low-frequency band when the transmission distance increases. Since the accumulated dispersion is varied by the length of SSMF, a multi-band signal can be allocated to different users by the transmission distance which can realize point-to-multipoint service for the SCM-based RoF system.

IV. Convolutional Neural Network

The simulation presented in section III exhibits the developed numerical model of the proposed filter can provide the insight of better understanding on designing the MPF. The parameters of the MPF can be decided through the simulation. For instance, the dispersive values should be determined firstly since it is related to the length of fiber which is hard to change in the practical system. Then, considering the given dispersive value, the wavelength spacing and the number of carriers are gradually adjusted to meet the desired requirement of the filter, respectively. The frequency response of the MPF can be obtained by the forward numerical model, $Y = f(X)$, which is derived from (19). The parameters and the sampled frequency response of the MPF are represented in the vector form, $X = [x_1, \ldots, x_n]$ and $Y = [y_1, \ldots, y_m]$ where n and m are the length of the input and output vectors, respectively. It is quite straight forward to design the MPF by tuning the parameters by the forward numerical model. However, these parameters are tuned separately, which is a time-consuming method and needs previous experience to optimize the performance. Moreover, diverse shapes of the MPF (i.e., frequency response) can be formed by varying the tap coefficients (i.e., the optical power of each optical carrier) [39]. If the tap coefficients are considered, the forward numerical model becomes more complex that increases the difficulty in designing the MPF. Therefore, finding an inverse function to directly determine all the MPF parameters (X) simultaneously by the given frequency response is more effective. Yet, it is difficult to figure out the inverse function between the frequency response and the

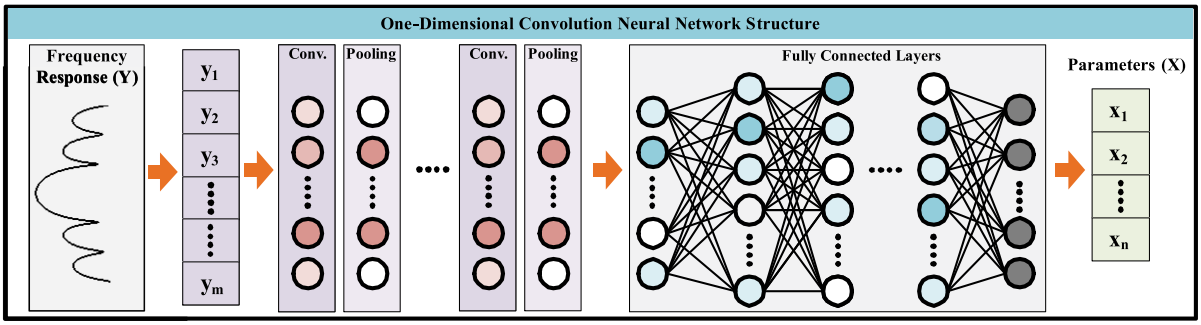

Fig. 7. The architecture of the proposed CNN model.

TABLE I
THE SUMMARIZATION OF THE PROPOSED CNN MODEL

Layer	Output Shape	Parameter
Conv_1D	(batch,2000,256)	1024
Activation (Relu)	(batch,2000,256)	0
Conv_1D	(batch,2000,256)	196864
Activation (Relu)	(batch,2000,256)	0
Max_Pooling_1D	(batch,667,256)	0
Global_Max_Pooling_1D	(batch,256)	0
Dense_1	(batch,2048)	526336
Dropout	(batch,2048)	0
Dense_2	(batch,256)	524544
Dense_3	(batch,128)	32896
Dense_4	(batch,1)	129

Total parameter:1281793
Trainable parameter:1281793
Non-trainable parameter:0

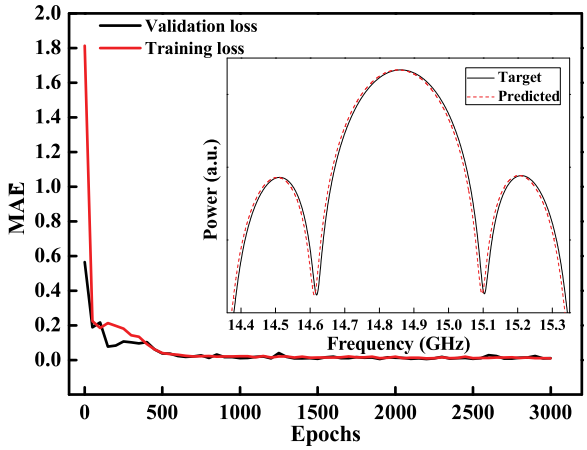

Fig. 8. MAE during the training and validation and the frequency response comparison between target and predicted data of first scenario.

complicated parameters of the MPF. (dispersive value, wavelength spacing, number of optical carriers, tap coefficients). Aside from the proposed MPF, other works encounter the same difficulty developing the inverse system. To address this issue, machine learning techniques featuring high accuracy, low complexity and fast, have been proposed to learn the inverse mapping between the output and input data [40]–[42]. The convolutional neural network (CNN) is a kind of deep neural network (DNN) architecture with a promising capability of extracting features from the input data and subsampling the data size which increases the execution efficiency. Additionally, the convolution operation of CNN is convenient to the one-dimensional vector. Therefore, many studies using 1D CNN structure have been proposed in different applications [43]–[45]. Since the frequency response of the MPF is a 1D vector, we adopt the CNN to find the inverse mapping between the output frequency response and the input parameters of the MPF which denotes as $\mathrm{X} = \mathrm{CNN(Y)}$, where CNN(.) is the inverse function generated by the CNN model. The proposed CNN architecture includes convolutional layers and fully connected layers as shown in Fig. 7. In the 1D CNN layers, the data are convolved by utilizing the kernels to extract the output features which can be expressed as [46]

$$x_k^l = b_k^l + \sum_{i=1}^{N_{l-1}} conv1D(w_{ik}^{l-1}, s_i^{l-1}) \tag{20}$$

where x_k^l is defined as the input, b_k^l is defined as the bias of the k^{th} neuron at layer l, $s_i^{l-1}$is the output of the i^{th} neuron at layer $l-1$, w_{ik}^{l-1} is the kernel from the i^{th} neuron at layer $l-1$ to the k^{th} neuron at layer l. $conv$1D (.,.) is used to perform 1D convolution with zero-padding. The intermediate output, y_k^l, can be expressed by passing the input x_k^l through the activation function, $\sigma(.)$, as

$$y_k^l = \sigma(x_k^l) \tag{21}$$

The Rectified Linear Unit (ReLU) is used as the activation function in the proposed CNN for increasing the computation efficiency [47], which acts individually on each of its input vector elements by keeping the positive values and equating the negative to zero. [48] Then the data size can be shortened by applying the down-sampling operation in the pooling layer which can be written as

$$s_k^l = y_k^l \downarrow ss \tag{22}$$

where s_k^l stands for the output of the k^{th} neuron of the layer, l, and "$\downarrow$ ss" represents the down-sampling operation with a scalar factor, ss. As the forward propagation is complete, the weights and bias are found. To improve the accuracy of the proposed CNN, the gradient descent algorithm is applied to update the weights and bias which is

$$\mathrm{X}^{\mathrm{Pred}}(t+1) = \mathrm{X}^{\mathrm{Pred}}(t) - \eta \nabla \mathrm{E}(\mathrm{X}^{\mathrm{Pred}}) \tag{23}$$

where $\mathrm{X}^{\mathrm{Pred}}$ is the predicted value, t is the iteration number and $\eta > 0$ is the learning rate. The mean absolute error (MAE) is used to define the error$\nabla \mathrm{E}(\mathrm{X}^{\mathrm{Pred}})$between the target and predicted

TABLE II
THE COMPARISON BETWEEN THE SELECTED TARGET AND PREDICTED DATA FOR BOTH SCENARIOS

	Target data	Predicted value
Scenario1	9.5GHz	9.50196 GHz
	10 GHz	10.0046 GHz
	10.5 GHz	10.5026 GHz
Scenario2	48 km	48.0170 km
	49 km	48.9792 km
	50 km	49.9474 km
	51 km	51.0164 km
	52 km	51.9649 km

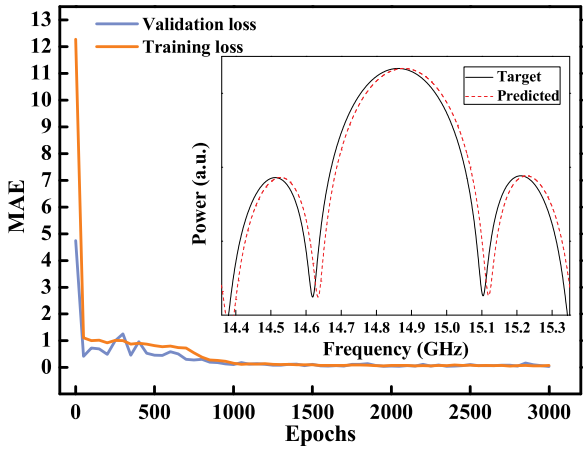

Fig. 9. MAE during the training and validation and the frequency response comparison between target and predicted data of second scenario.

data. The learning rate η is dynamically adapted by using the Adam optimizer [49] which can enhance the convergence during the training process.

To demonstrate the concept of designing the MPF by the machine learning technique, the CNN model is utilized to learn the inverse mapping between the frequency response of the MPF and wavelength spacing and fiber length, respectively.

To collect the training data, the frequency responses within the frequency range from 14 GHz to 16 GHz are sampled by 2000 points using the theoretical model of the proposed MPF in section III. For the first scenario, predicting the wavelength spacing, 2485 datasets of frequency responses are generated by varying the wavelength spacing from 5 GHz to 20 GHz (with 60 optical carriers and the equivalent dispersive value as 50-km fiber). The second scenario, to predict the fiber length, 2485 datasets are collected by changing the fiber length from 46 to 53 km (with 60 optical carriers and the wavelength spacing of 10 GHz). For both scenarios, 10% of the data are designated to be the testing data and the training data to validation data ratio is set to 7:3. By optimizing the model parameters, such as epochs, convolution layers, hidden layers, batches, and activation function, the CNN architecture as shown in Table I is obtained. The training data are first convolved by 256 kernels and fed into the rectified linear unit (RELU) layer to normalize the value. Then, the first RELU layer is connected to the second convolutional layer and RELU layer in sequence. Afterward, a max pooling layer with the window size of 3 down-samples the data and sends the output to the fully connected layers, including three hidden layers that have 2048, 256, 128 neurons, respectively.

Fig. 8 shows the loss plot and the effect of the number of epochs during CNN model training. The training losses are reduced as the number of epochs increases. The training loss and validation loss converge quickly after approximately 500 epochs, while the optimum validation MAE of 0.004522 is achieved at the 2158th epoch. The predicted and target frequency responses of the 10 GHz wavelength spacing are plotted in the inset of Fig. 8. The predicted value is 10.0046 GHz as listed in Table II. Moreover, Table II lists the other selected wavelength spacing values to make a straight comparison between predicted and target data. The MAE of 248 testing datasets is 0.015516.

Fig. 9 illustrates the training loss curve of the second scenario. The training and validation data converge around the 800th epoch and the optimal validation MAE is 0.026744. The predicted values of five selected testing data are listed in Table II and the inset of Fig. 9 shows the target and predicted frequency responses of the 50-km fiber length. The testing MAE among 248 datasets is 0.060804. According to the insets of Fig. 8 and Fig. 9, the results present good matches between the target and predicted frequency responses for both scenarios and the low testing MAE values indicate the proposed CNN model has good performance in this demonstration.

V. CONCLUSION

In this paper, the CNN model is utilized to predict the wavelength spacing and fiber length for microwave photonic filter design. The centralized-reconfigurable filter is composed of an optical comb generator and a PM. Experimental results show that the proposed comb generator can generate 20,40,60,80 and 100 optical carriers by adjusting the optical filter which exhibits a good flatness and high TNR. Additionally, by changing the frequency of LO, optical carriers with different wavelength spacing are also successfully demonstrated. With good performance of the optical carriers, large flexibility of the proposed filter is achieved. The center frequency of the proposed filter can be shifted from 14.08 to 15.66 GHz when the wavelength spacing is tuned from 0.084 nm to 0.076 nm and the 3-dB bandwidth decreases from 744.8 MHz to 306.8 MHz when the number of optical carriers increases from 20 to 60. Furthermore, theoretical analysis and numerical simulations are complete and they are consistent with the experimental results. Moreover, we have simulated the point-to-multipoint application of the proposed filter by setting the length of SSMF. With the full study on the proposed filter, we further collect the data with two different scenarios to train the CNN model which is used to successfully predict the wavelength spacing and the fiber length with only small errors, exhibiting good performance

and high accuracy of the proposed model. Our proposed MPF design enhanced by CNN machine learning technique, can be further improved by collecting more training data and utilizing advanced optimization algorithms for radio-over-fiber mobile network applications.

REFERENCES

[1] L. R. Chen and V. Page, "Tunable photonic microwave filter using semiconductor fiber laser," *Electron. Lett.*, vol. 41, no. 21, pp. 1183–1184, 2005.

[2] M. I. Comanici, L. R. Chen, and P. Kung, "Microwave photonic filter-based interrogation system for multiple fiber Bragg grating sensors," *Appl. Opt.*, vol. 56, pp. 9074–9078, 2017.

[3] J. Capmany, I. Gasulla, and D. Pérez, "Microwave photonics: The programmable processor," *Nat. Photon.*, vol. 10, no. 1, pp. 6–8, Jan. 2016.

[4] M. Li and N. Zhu, "Recent advances in microwave photonics," *Frontiers Optoelectron*., pp. 160–185, Jun. 2016.

[5] C. H. Lee, *Microwave Photonics*. Boca Raton, FL, USA: CRC, 2007.

[6] R. K. Shiu *et al.*, "Tunable microwave photonic filter for millimeter-wave mobile fronthaul systems," in *Proc. IEEE Photon. Conf.*, 2018, pp. 1–2.

[7] M. Li and N. Zhu, "Recent advances in microwave photonics," *Front. Optoelectron.*, vol. 9, no. 2, pp. 160–185, 2016.

[8] R. A. Minasian, E. H. W. Chan, and X. Yi, "Microwave photonic signal processing," *Opt. Exp.*, vol. 21, no. 19, pp. 14921–14935, 2013.

[9] C. H. Chang *et al.*, "A distribute feedback laser diode composed microwave photonic bandpass filter for SCM based optical transport systems," *IEEE J. Sel. Topics Quantum Electron.*, vol. 21, no. 6, 2015, Art no. 1503506.

[10] H. Fu and K. Zhu, "Radio-over-fiber system with multiple-optical-source-based microwave photonic filter performing as a subcarrier demultiplexer," *IEEE Photon. J.*, vol. 3, no. 2, pp. 152–157, 2011.

[11] J. Ge and M. P. Fok, "Passband switchable microwave photonic multiband filter," *Sci. Rep.*, vol. 5, 2015, Art no. 15882.

[12] H. Y. Fu, Z. W. Xu, and K. Zhu, "Remote wideband microwave frequency measurement based on a single-passband microwave photonic filter," *IEEE Photon. J.*, vol. 4, no. 5, pp. 1401–1406, 2012.

[13] F. Jiang, Y. Yu, H. Tang, L. Xu, and X. Zhang, "Tunable band-pass microwave photonic filter with ultrahigh stopband attenuation and skirt selectivity," *Opt. Exp.*, vol. 24, no. 16, pp. 18655–18663, 2016.

[14] L. W. Li, X. K. Yi, T. X. H. Huang, and R. A. Minasian, "Shifted dispersion-induced radio-frequency fading in microwave photonic filters using a dual-input Mach–Zehnder electro-optic modulator," *Opt. Lett.*, vol. 38, no. 7, pp. 1164–1166, 2013.

[15] W. Li, N. H. Zhu, and L. X. Wang, "Brillouin-assisted micro-wave frequency measurement with adjustable measurement range and resolution," *Opt. Lett.*, vol. 37, no. 2, pp. 166–168. 2012.

[16] D. Marpaung *et al.*, "Si 3 N 4 ring resonator-based microwave photonic notch filter with an ultrahigh peak rejection," *Opt. Exp.*, vol. 21, no. 20, pp. 23286–23294, 2013.

[17] J. Wu *et al.*, "Passive silicon photonic devices for microwave photonic signal processing," *Opt. Commun.*, vol. 373, pp. 44–52, 2016.

[18] X. Liu, Y. Yu, H. Tang, L., Xu, J., Dong, and X., Zhang, "Silicon-on-insulator-based microwave photonic filter with narrowband and ultrahigh peak rejection," *Opt. Lett.*, vol. 43, no. 6, pp. 1359–1362, 2018.

[19] Z. Wang *et al.*, "Frequency comb generation using a CMOS compatible SiP DD-MZM for flexible networks," *Photon. Technol. Lett.*, vol. 30, pp. 1495–1498, 2018.

[20] M. S. Alshaykh, J. D. Mckinney, and A. M. Weiner, "Radio-frequency signal processing using optical frequency combs," *Photon. Technol. Lett.*, vol. 31, no. 23, pp. 1874–1877, 2019.

[21] C. H. Yeh, Z. Q. Yang, T. J. Huang, C. W. Chow, J. H. Chen, and K. H. Chen, "Wavelength-selectable and steady single-mode erbium-doped fiber multiple ring laser," *Laser Phys*., vol. 27, 2017, Art no. 115104

[22] P. C. Peng *et al.*, "Multiwavelength fiber laser using S-band erbium-doped fiber amplifier and semiconductor optical amplifier," *Opt. Commun.*, vol. 259, no. 1, pp. 200–203, 2006.

[23] J. Wu *et al.*, "RF photonics: An optical microcombs' perspective," *IEEE J. Sel. Topics Quantum Electron.*, vol. 24, no. 4, pp. 1–20, 2018.

[24] H. Shahoei and J. Yao, "A continuously tunable multi-tap com-plexcoefficient microwave photonic filter based on a tilted fiber Bragg grating," *Opt. Exp.*, vol. 21, no. 6, pp. 7521–7527, 2013.

[25] J. Lloret *et al.*, "Tunable complex-valued multi-tap microwave photonic filter based on single silicon-on insulator microring resonator," *Opt. Exp.*, vol. 19, no. 13, pp. 12402–12407, 2011.

[26] X. Xu *et al.*, "Advanced RF and microwave functions based on an integrated optical frequency comb source," *Opt Express*, vol. 26, pp. 2569–2583, 2018.

[27] K. K. Loh, K. S. Yeo, Y. G. Shee, F. R. M. Adikan, and M. A. Mahdi, "Microwave photonic filter using multiwavelength Brillouin-erbium fiber laser," *IEEE Photon. Technol. Lett.*, vol. 27, no. 1, pp. 65–68, 2015.

[28] Z. Li, V.K.S. Hsiao, Z. Chen, J.Y Tang, F.L. Zhao, and H. Z. Wang, "Optically tunable fiber bragg grating," *IEEE Photon. Technol. Lett.*, vol. 22, no. 15, pp. 1123–1125, 2010.

[29] M. Tornatore, G.-K. Chang, and G. Ellinas, *Fiber-Wireless Convergence in Next-Generation Communication Networks: Systems, Architectures, and Management*. Springer, 2017

[30] G. Keiser, *Optical Fiber Communication*. New York, NY, USA: McGrawHill, Sep .2013.

[31] S. Donati and V. Annovazzi-Lodi, "From order to chaos and back: Recent advances in optical cryptography of transmitted data," in *Proc. Int. Conf. Adv. Optoelectron. Lasers*, Sep. 2013, pp. 1–6.

[32] Q. Zhou *et al.*, "Enhanced multi-level signal recovery in mobile fronthaul network using DNN decoder," *IEEE Photon. Technol. Let*, vol. 30, no. 17, pp. 1511–1514, Sept. 2018.

[33] J. He *et al.*, "Demonstration of high precision 3D indoor positioning system based on two-layer ANN machine learning technique," in *Proc. Opt. Fiber Commun. Conf. (OFC)*, 2019, pp. 1–3.

[34] Y. C. Manie *et al.*, "Enhancement of the multiplexing capacity and measurement accuracy of FBG sensor system using IWDM technique and deep learning algorithm," *J. Lightw. Technol.*, vol. 38, no. 6, pp. 1589–1603, 2020.

[35] S. Liu, P. C. Peng, L. Huang, C. W. Hsu, H. Tian, and G.K. Chang, "Bandwidth-enhanced PAM-4 transmissions using polarization modulation and direct detection with a tunable frequency range," *J. Lightw. Technol.*, vol. 37, no. 3, pp. 1014–1022, 2019.

[36] C. W. Chow and C. H. Yeh, "Mitigation of Rayleigh backscattering in 10-Gb/s downstream and 2.5-Gb/s upstream DWDM 100-km long-reach PONs," *Opt. Exp.*, vol. 19, no. 6, pp. 4970–4976, 2011.

[37] F. Zeng and J. P. Yao, "Investigation of phase-modulator-based all-optical bandpass microwave filter," *J. Lightw. Technol.*, vol. 23, no. 4, pp. 1721–1728, 2005.

[38] X. Xu *et al.*, "Advanced adaptive photonic RF filters with 80 taps based on an integrated optical micro-comb source," *J. Lightw. Technol.*, vol. 37, no. 4, pp. 1288–1295, 2019.

[39] X. Xu *et al.*, "High performance RF filters via bandwidth scaling with Kerr Micro-Combs," *APL Photon*., vol. 4, no. 2, 2019, Art. no. 026102.

[40] D. Zibar, A. M. Rosa Brusin, U. C. de Moura, F. Da Ros, V. Curri, and A. Carena, "Inverse system design using machine learning: The Raman amplifier case," *J. Lightw. Technol.*, vol. 38, no. 4, pp. 736–753, 15 Feb. 15, 2020.

[41] Y. Chen, J. Du, Y. Huang, K. Xu, and Z. He, "Intelligent gain flattening of FMF Raman amplification by machine learning based inverse design," in *Proc. Opt. Fiber Commun. Conf.*, 2020, pp. 1–3.

[42] B. Li *et al.*, "Robust convolutional neural network model for wavelength detection in overlapping fiber Bragg grating sensor network," in *Proc. Opt. Fiber Commun. Conf.*, 2020, pp. 1–3.

[43] M. Özdeş and B. M. Severoğlu, "Sound spectrum detection using deep learning," in *2019 Scientific Meeting on Electrical-Electronics & Biomedical Engineering and Computer Science*, 2019, pp. 1–4.

[44] S. Kiranyaz, T. Ince, R. Hamila, and M. Gabbouj, "Convolutional neural networks for patient-specific ECG classification," in *Proc. 37th Annu. Int. Conf. Eng. Med. Biol. Soc.*, 2015, pp. 2608–2611.

[45] Y. Lu, Z. Wang, R. Xie, and S. Liang, "Bayesian optimized deep convolutional network for electrochemical drilling process," *J. Manuf. Mater. Process.*, vol. 3, 2019, Art no. 53.

[46] S. Kiranyaz, A. Gastli, L. Ben-Brahim, N. AlEmadi, and M. Gabbouj, "Real-time fault detection and identification for MMC using 1-D convolutional neural networks," *IEEE Trans. Ind. Electron.*, vol. 66, no. 11, pp. 8760–8771, 2019.

[47] Krizhevsky, I. Sutskever and G. E. Hinton, "ImageNet classification with deep convolutional neural networks",in *Proc. Adv. Neural Inf. Process. Syst.*, pp. 1097–1105, 2012.

[48] Karanov *et al.*, "End-to-end deep learning of optical fiber communications," *J. Lightw. Technol.*,vol. 36, no. 20, pp. 4843–4855, 2018.

[49] Kingma, J. Ba, "Adam: A method for stochastic optimization," 2014.